Development of Frequency-Dependent DC Equivalent Models for Multi-Terminal DC Grids

Mohamed Elsodany[a,b,*], Kosei Shinoda[a], Jing Dai[a,c,d] and Seddik Bacha[e,a]

[a] SuperGrid Institute, Villeurbanne, France
[b] Université Grenoble Alpes, Grenoble, France
[c] Université Paris Saclay, Gif-sur-Yvette, France
[d] Sorbonne Université, Paris, France
[e] Univ.Guyane, Cayenne, French Guiana

ARTICLE INFO

Keywords:
HVDC transmission
Interoperability
Modular Multilevel converter
small-signal analysis

ABSTRACT

The emergence of Multi-Terminal DC (MTDC) grids for offshore wind integration introduces challenges in modeling dynamic interactions and ensuring HVDC system stability. Accurate AC and DC grid equivalents are essential for converter compliance testing and control design, especially in a multi-vendor context, where interoperability issues may arise. This paper proposes two DC grid equivalent models: a simple RLC-based model for low-frequency dynamics, and a reduced-order frequency-dependent model (from order 47 to 5) to capture both low and high frequency behavior based on DC-grid impedance fitting. The two models can effectively capture different DC grid variations, such as variations in DC Reactor (DCR) size, control modes, and operating points. Their applicability is demonstrated through frequency-domain impedance analysis and time-domain simulations of a 3-terminal DC grid with detailed MMC models. A case study is presented to highlight the importance of representing higher frequency dynamics for stability analysis. In addition, the frequency-dependent model is implemented in time-domain simulations to bridge the gap between stability analysis in the frequency and time domains.

1. Introduction

With the increasing integration of renewable energy sources, especially offshore wind farms, Multi-Terminal DC (MTDC) grids are recognized as a flexible solution for bulk power transmission over long distances. Compared to the existing point-to-point HVDC links, an MTDC grid offers multiple advantages, including increased reliability, reduced losses, and improved power quality [1].

To analyze the control interactions between converter stations in an MTDC grid, stability studies are typically conducted to identify the undamped resonant modes and to propose mitigation measures. Several stability studies of MTDC grids have been reported in the literature, either based on eigenvalue analysis [2, 3, 4] or frequency-domain impedance analysis [5, 6, 7]. Most of these studies are conducted based on the full knowledge of the system configuration and the elements of the DC grid. However, in practice, the converter control design is often performed at an early stage of an HVDC project, when the grid configuration is not yet finalized. This may lead to interoperability issues when the converter is connected to a DC grid comprising different vendors' converters and components.

To address this challenge, the concept of grid equivalents has been widely adopted in AC systems. A simple representation of the AC grid by a Thevenin equivalent is typically utilized, consisting of an ideal AC voltage source v_{ac}^{nom} behind an impedance Z_{ac}, giving an indication of the AC system's short-circuit power. The AC grid can further be represented as frequency-dependent impedance models using vector fitting methods, especially with the need to capture higher frequency dynamics [8, 9, 10, 11]. According to [12], the relevant system operator is required to provide representative AC network equivalents that describe the grid behavior at the AC Point of Connection (AC-PoC), which simplifies both the converter control design and compliance process, ensuring that no instability issues arise when the converter is connected to the grid.

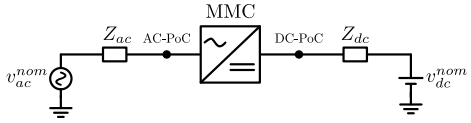

Figure 1: Equivalent representation of the AC and DC grids at the AC-PoC and DC-PoC, respectively.

In the literature, the representation of the DC system has often been based on oversimplifying hypotheses [2, 3, 13, 14, 15, 16]. For example, an ideal DC voltage source is typically considered when testing the active power response of a converter, while an ideal DC current source is often used to test the DC voltage control of the converter. Such simplifications do not accurately represent the actual DC grid. Consequently, the converter response in reality may turn out to be significantly different from the results obtained during the control design stage. To the knowledge of the authors, only [17] has investigated different DC-system models for the proper design of converter control. The authors focused on the risk of converter model reduction, which may lead to instability for some controller tuning conditions. However, the study did not provide further insight into other factors

*Corresponding author
mohamed.elsodany@g2elab.grenoble-inp.fr (M. Elsodany)
ORCID(s):

influencing the DC grid impedance, such as the DC reactor size.

This paper aims first to provide a deeper insight into DC grid behavior, similar to the research efforts conducted for AC system representation. We then propose two equivalent models for a given DC grid, following the same structure of the AC grid representation, as in Fig. 1. The first model is a simplified one that captures the dominant low-frequency dynamics of the DC system, while the second one is a detailed model that captures the frequency-dependent nature of the grid impedance. Moreover, the frequency-dependent equivalent is implemented in the time domain, which shall fill the gap between the frequency-domain and the time-domain stability analyses. The two proposed models are compared and validated against a reference three-terminal DC grid model, with detailed MMC dynamics in both frequency domain and time domain. Their respective advantages, disadvantages, and key applications are highlighted and discussed.

The rest of this paper is structured as follows: Section 2 introduces the DC grid model with the MMC and cable details, and outlines the approach for deriving the grid impedance at the DC Point of Connection (DC-PoC). Key factors influencing the dynamic behavior of the DC grid are investigated in Section 3. Building on this analysis, two solutions for representing the DC grid are proposed in Section 4. The effectiveness of these representations is demonstrated through a case study of a 3-terminal DC grid in Section 5. Section 6 concludes the paper by summarizing the findings and insights.

2. DC-grid impedance model development

2.1. System modeling

We consider the 3-terminal asymmetrical monopolar DC grid depicted in Fig. 2, which consists of two onshore stations, Stations 1 and 2, and one offshore station, Station 3. The MMCs are interconnected by two 100 km DC cables, respectively between Stations 1 and 2, and Stations 2 and 3.

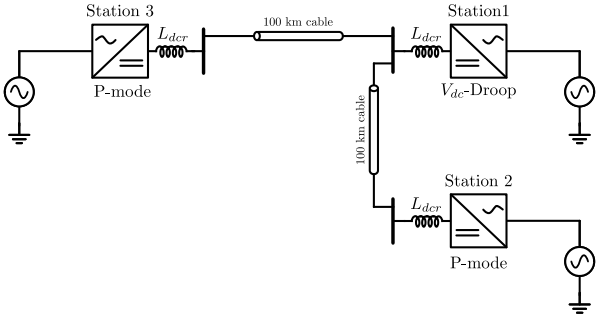

Figure 2: 3-terminal asymmetrical monopolar DC grid under study.

The MMC Arm Average (AAM) model [18, 19] is considered in this paper for the representation of converter stations. Each arm is represented by an equivalent capacitor, as shown in Fig. 3. The modeling of each MMC follows the approach presented in [20], where the internal dynamics are represented in multiple dq frames to obtain time-invariant variables. The general cascaded control structure of the MMC in Fig. 4 is considered, where the outer control (P-control or Vdc-control) provides the reference for the inner control (d-axis current reference). The reactive power control is out of the scope of this paper, and hence the q-axis current reference is set to 0 in the rest of this study. The output of the current control provides references for the inserted voltages for lower-level control. A pair of PI controllers are used to suppress the circulating currents, as proposed in [21]. The derivation of the MMC dynamics can be found in Appendix A.

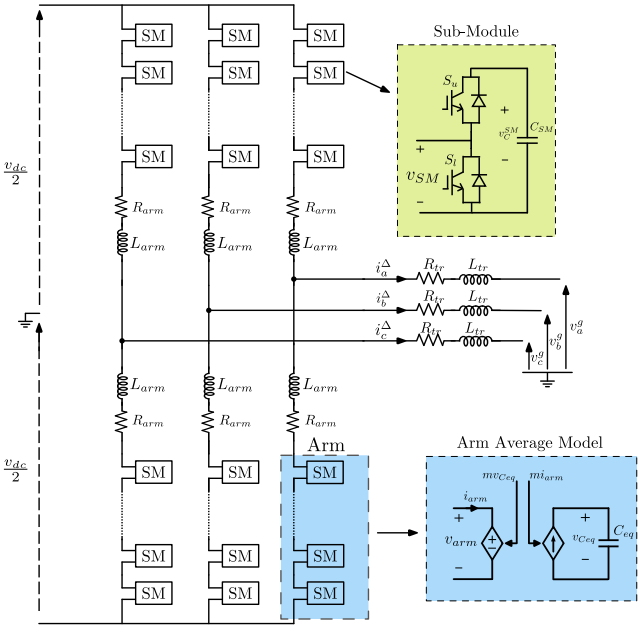

Figure 3: A schematic of the Modular Multilevel Converter (MMC) and its Arm Average Model (AAM).

DC cables are modeled in state space using the method described in [22], where each cable is represented by a single π-section with three parallel RL branches, as shown in Fig. 5. This approach effectively captures the cable's frequency-dependent behavior and provides sufficient accuracy up to 300 Hz, which covers the frequency range relevant for the stability studies in this paper. The cable parameters are based on a typical XLPE HVDC cable, with data adapted from [23].

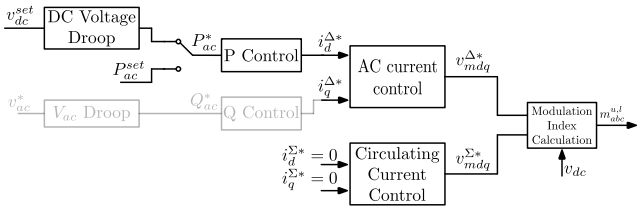

Figure 4: MMC control structure.

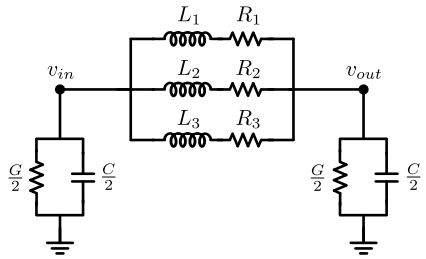

Figure 5: Cable model of a single π section with three parallel RL branches [22].

Table 1
Grid parameters.

Parameter	Value
Nominal power [MVA]	1000
Nominal DC voltage [kV]	525
Nominal AC voltage [kV]	400 RMS L-L
Transformer resistance [pu]	0.5%
Transformer inductance [pu]	18%
MMC arm inductance [pu]	15%
MMC arm capacitance [μF]	48.4

DC reactors (DCRs) are critical components for limiting fault currents in DC grids. They can be installed at the terminals of converter stations or as part of the DC circuit breaker system, enabling selective protection strategies [24]. In this study, a DC reactor is added at the terminals of each converter station.

Additional grid parameters are given in Table 1. The closed-loop state-space model of the grid is obtained by aggregating that of the MMCs, the cables, and the DC reactors using the component connection method [25].

2.2. Methodology: small-signal analysis

From the state-space model described above and detailed in Appendix A, we derive a frequency-dependent small-signal model to represent the grid impedance at the DC-PoC. In particular, by choosing the DC voltage as the input and the DC current as the output, the DC-side impedance can readily be deduced from the state-space model obtained in Section 2.1. The grid impedance Z_{grid} thus obtained can be easily interconnected with the converter DC-side admittance Y_{MMC} to analyze the small-signal stability of the closed-loop system in the frequency domain. Fig. 6 shows the methodology used in this process.

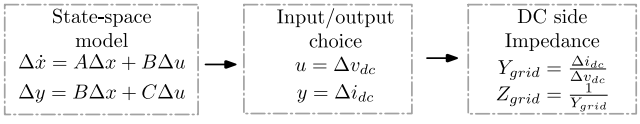

Figure 6: Methodology to derive the DC grid impedance at the DC-PoC from the corresponding state-space representation.

To validate the impedance model derived for the grid in Fig. 2, a frequency scan is conducted using the nonlinear model in EMTP-RV. The cable model parameters are adapted from [23]. A small voltage perturbation at multiple frequencies is injected into the grid, and a Fast Fourier Transform (FFT) is applied to the DC current response to obtain the magnitude and phase angle at each frequency. The equivalent grid admittance is then computed using the frequency-domain input/output relationship: $Y_{grid}(\omega) = I_{dc}(\omega)/V_{dc}(\omega)$. Thus, the grid impedance is obtained as the inverse of the admittance $Z_{grid}(\omega) = \frac{1}{Y_{grid}(\omega)}$. The overall setup for the scanning process is shown in Fig. 7.

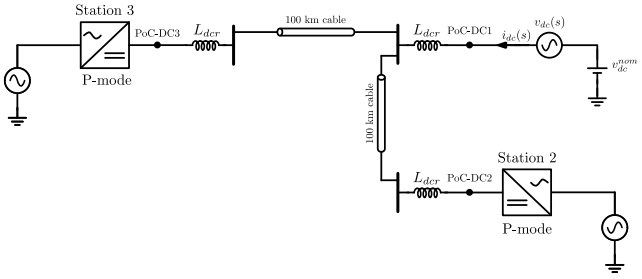

Figure 7: Frequency scan setup to obtain the DC grid impedance at DC-PoC1.

Fig. 8 shows that the grid impedance is accurately captured by the analytical model, which reflects the different resonances observed in the frequency scan results. In the very low-frequency range below 10 Hz, the grid exhibits capacitive behavior, characterized by a decreasing magnitude and a phase angle of -90°. Around 10 Hz, a resonance occurs when the grid impedance magnitude reaches a minimum. In the high-frequency range above 110 Hz, the grid impedance is dominated by inductive behavior, represented by an increasing magnitude and a phase angle of 90°. The mid-frequency resonances result from the combined dynamics of the cable and the MMC.

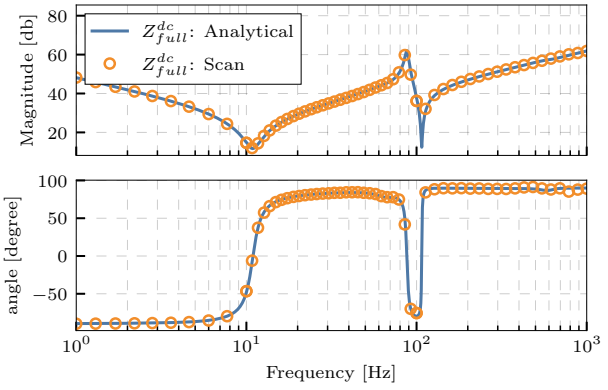

Figure 8: Comparison between the analytically derived grid impedance and the frequency scan result.

3. Sensitivity study of the grid impedance at the DC point of connection

In this section, a sensitivity analysis is conducted to investigate the parameters impacting the DC grid impedance

at the DC-PoC. To thoroughly capture the behavior of the grid impedance, we investigate the influence of both the passive components of the DC grid and the control mode of the remote MMC stations.

Initially, the DCR size of all stations is 200 mH. Stations 2 & 3 operate in constant P-mode with no power exchange in steady state. The influence of the following aspects is investigated.

3.1. Impact of the DC reactor size

The effect of the DCR size is analyzed by testing three different values for all DCRs. The resulting grid impedance in Fig. 9 shows that larger DCRs reduce the frequency of the resonances at both low and high frequencies. For the dominant low-frequency resonance around 10 Hz, the impedance magnitude is lower for larger DCRs, indicating lower damping for this resonance, which is in line with the conclusions in [26].

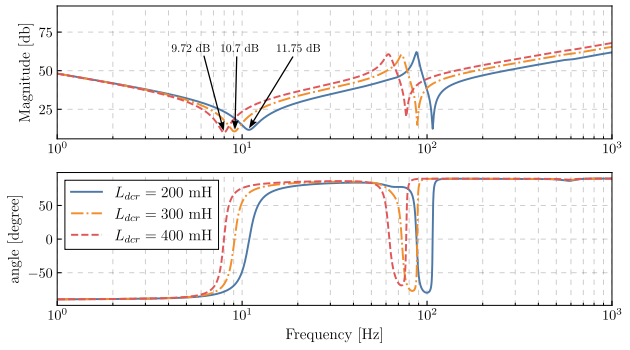

Figure 9: Impact of DCR size on the grid impedance seen at DC-PoC1.

To distinguish the impact of the DCR in the vicinity of the DC-PoC from that of the DCRs installed at a considerable distance from the DC-PoC under investigation, we first change only the size of the DCR directly connected to DC-PoC1, and then only the size of the DCR connected to DC-PoC2 and DC-PoC3. The results in Fig. 10 indicate that the impact of the nearby DCR is more noticeable in the high-frequency range, whereas the effect of the remote DCRs of remote stations is only pronounced at low frequencies. This leads to the conclusion that high-frequency dynamics are primarily a local phenomenon, with the nearby DCR filtering out high-frequency dynamics originating from distant stations.

3.2. Impact of the operating point

Given the nonlinear nature of the closed-loop system under study, the grid impedance is influenced by the equilibrium point around which the linearization is performed, which also corresponds to the initial DC power flow. To better understand its effect, note that the low-frequency behavior of an MMC operating in constant P-mode can be approximated as an ideal power source. In this mode, the MMC regulates the output DC current to maintain a constant power output P_0 regardless of changes in the voltage across

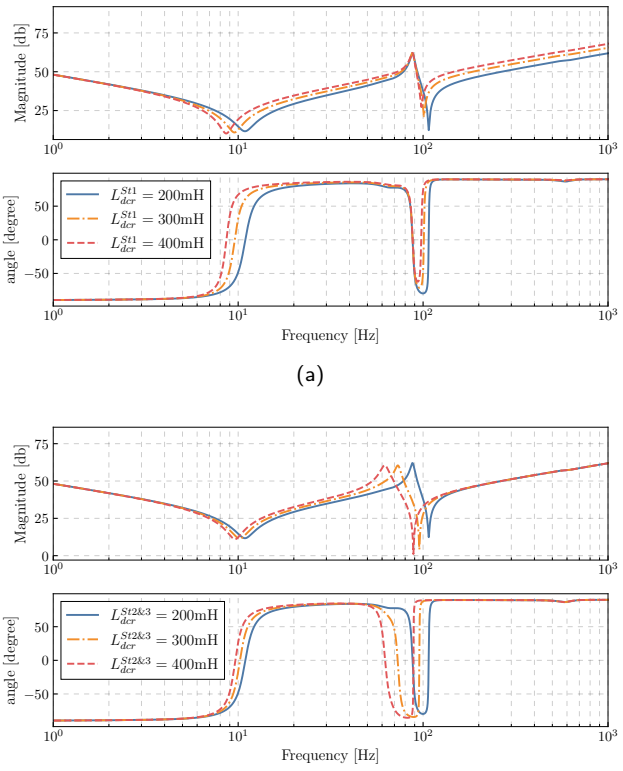

Figure 10: Impact of the DCR size: (a) Changing only L_{dcr}^{St1}, with L_{dcr}^{St2} and L_{dcr}^{St3} maintained at 200 mH and (b) Changing only L_{dcr}^{St2} and L_{dcr}^{St3}, with L_{dcr}^{St1} maintained at 200 mH.

the capacitor C, which represents its internal stored energy, as illustrated in Fig. 11. The governing equation for this simplified MMC model is:

$$C\frac{dv_{dc}(t)}{dt} = i_{dc}(t) - \frac{P_0}{v_{dc}(t)} \tag{1}$$

By linearizing (1), the MMC impedance can be obtained as

$$Z_{MMC}(s) = \frac{\Delta V_{dc}(s)}{\Delta I_{dc}(s)} = \frac{1}{sC - \frac{P_0}{v_{dc0}^2}} \tag{2}$$

Equation (2) shows that, when $P_0 = 0$, the MMC behaves as a capacitor at low frequencies, with a decreasing impedance magnitude and a phase angle of -90°. If $P_0 < 0$ (i.e. operation in rectifier mode), the MMC is dominated by a positive impedance with a constant magnitude and a phase angle of 0°. Finally, if $P_0 > 0$ (i.e. operation in inverter mode), the low-frequency behavior is dominated by a negative impedance with a constant magnitude and a phase angle of 180°, demonstrating the constant power load behavior [27].

To verify the above analysis, the grid impedance seen at DC-PoC1 is derived at three different initial operating points:

1. At op1, $P_2 = P_3 = 0$ pu.

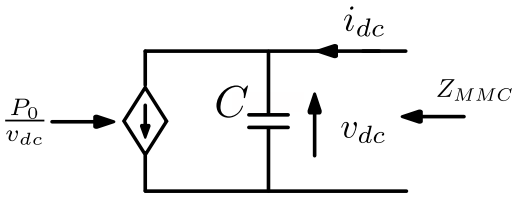

Figure 11: Simplified MMC model operating in constant P-mode.

2. At op2, $P_2 = P_3 = -0.5$ pu. (both stations in rectifier mode).
3. At op3, $P_2 = P_3 = 0.5$ pu. (both stations in inverter mode).

The results in Fig. 12 indicate that the grid impedance at low frequencies is primarily influenced by the operating point of the distant MMCs. At op1, where both remote stations operate at zero power, the grid impedance exhibits capacitive behavior at low frequencies. At op2, where both remote stations operate in rectifier mode, the grid impedance shows resistive behavior with a constant magnitude and a phase angle of 0°. Finally, at op3, where both remote stations operate in inverter mode, the grid impedance displays negative resistive behavior with a constant magnitude and a phase angle of 180°. These observations are consistent with the previous analysis. On the other hand, the high-frequency grid behavior is not impacted by the operating point, where the the impedance response at the three operating points are nearly identical.

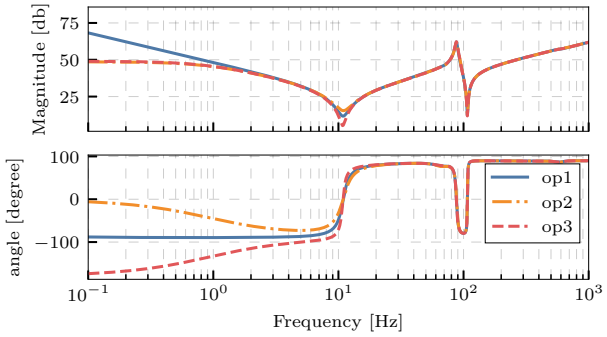

Figure 12: Grid impedance seen at DC-PoC1 for different operating points.

3.3. Impact of the control mode of remote stations

The participation of remote stations in regulating the DC voltage can alter the grid impedance observed at the DC-PoC. We consider two cases of control modes for the remote stations. In Case 1, both Stations 2 and 3 are in P-mode, while in Case 2, Station 2 operates in Vdc-droop control mode with a droop gain $k_d = 0.1$ pu, and Station 3 remains in P-mode. In both cases, the zero power operating point is considered (op1 in Section 3.2).

The results in Fig. 13 show that the control mode of Station 2 significantly affects the low-frequency range. Considering the low-frequency resonance around 10 Hz, the grid impedance magnitude is notably higher in Case 2, where Station 2 operates in DC-voltage droop mode, compared to Case 1, where it operates in P-mode. This indicates that the droop control mimics a resistive behavior in the low-frequency range, with a higher impedance magnitude that improves the damping of the DC voltage. This impact will be further analyzed in Section 4. However, since DC voltage droop control is a higher-level control, its influence is limited to frequencies below approximately 20 Hz and does not significantly affect the grid impedance at higher frequencies.

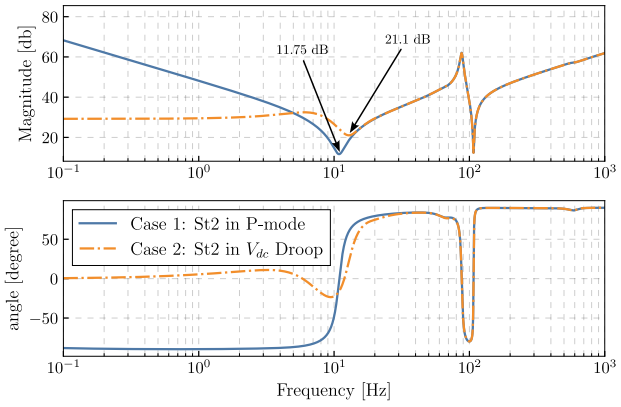

Figure 13: Impact of the control mode of Station 2 on the grid impedance at DC-PoC1.

To analyze the impact of the operating point of the grid when DC voltage droop control is applied to Station 2, we consider the same three operating points as in Section 3.2. The results shown in Fig. 14 indicate that, unlike the case where Station 2 operates in P-mode (Fig. 12), the low-frequency grid impedance is dominated by the action of the DC voltage droop control. This is evident in the figure, where the low-frequency response tends toward a constant magnitude and a phase angle of 0° across all operating points, indicating resistive behavior as the frequency decreases.

These observations further confirm that DC voltage droop control improves the damping at low frequency. It can also be noted that the operating point still has some influence on the low-frequency resonance, with op3 exhibiting a slightly lower impedance magnitude at the resonance frequency. Finally, the operating point has no impact on the high-frequency range, which is consistent with previous results in Section 3.2.

3.4. Impact of cable length

The influence of cable length on the grid impedance is analyzed by varying the lengths of both cables from 50 km to 300 km, while keeping other parameters unchanged. The results in Fig. 15 indicate that increasing the cable length most significantly affects the frequency response in the mid-frequency range, specifically between 50 Hz and 200 Hz. As the cable length increases, the series and parallel resonances

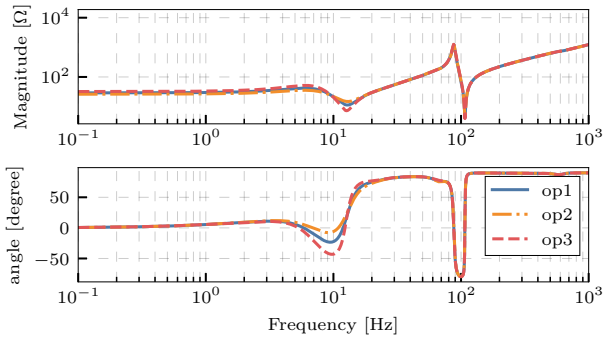

Figure 14: Impact of the operating point on the grid impedance at DC-PoC1 when Station 2 operates in Vdc-droop control mode.

in this range become more damped (more attenuation of the resonance peaks), and the resonance frequencies shift to lower values (shift to the left). Increasing the cable length also impacts the low-frequency range, where the series resonance around 10 Hz becomes more damped. However, the cable length has a negligible effect on the high-frequency range above 200 Hz, where the grid impedance is primarily influenced by the DCR nearest to the DC-PoC, as discussed in Section 3.1.

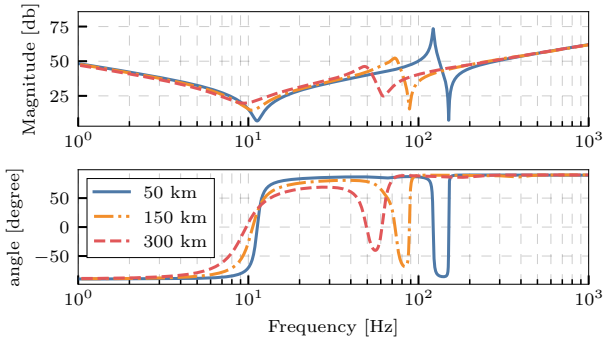

Figure 15: Impact of cable length on the grid impedance at DC-PoC1.

4. Development of the Equivalent Grid Model

The previous section showed that the grid impedance at the DC-PoC is significantly influenced by the DC reactors, the operating point, cable length, and the control mode of the remote stations. Thus, representing the grid impedance in a simplified form is essential for the design of the converter control.

In this section, we investigate two possible approaches yielding two respective models for representing the grid impedance at the DC-PoC. The choice between the two would depend on the required level of accuracy, and the available grid information. The first model is a simple RLC equivalent model, while the second model is a frequency-dependent equivalent model that can accurately capture the DC grid dynamics across wider frequency ranges.

4.1. RLC equivalent model

The RLC equivalent model provides a simple representation of the grid impedance at the DC-PoC. This model combines a series resistance R, inductance L, and capacitance C, as shown in Fig. 16. The values of the RLC parameters can be selected to represent the low-frequency resonance of the grid.

$$Z^{dc}_{eq1}(s) = R + sL + \frac{1}{sC - \frac{P_0}{v^2_{dc0}}} \tag{3}$$

Notice that the third term of (3) is the impedance of the MMC in P-mode, as derived in (2), where P_0 and v_{dc0} are the initial DC power and voltage, respectively. L represents the inductance present in the DC grid, and R represents the resistive losses in the grid, which also provides damping to the system. Equation (3) can be rearranged as

$$Z^{dc}_{eq1}(s) = \frac{s^2LC + s\left(RC - \frac{LP_0}{v^2_{dc0}}\right) + 1 - \frac{RP_0}{v^2_{dc0}}}{sC - \frac{P_0}{v^2_{dc0}}} \tag{4}$$

Equation (4) represents a transfer function with a pole at $s = \frac{P_0}{Cv^2_{dc0}}$ and a pair of zeros that depend on the operating point (P_0, v_{dc0}) and the RLC parameters.

To select the RLC parameters, the capacitor C is chosen to represent the aggregated capacitance of the grid shown in Fig. 2, where the equivalent MMC capacitance is given by $C_{MMC} = 6C_{arm}$, with C_{arm} being the MMC arm capacitance obtained from Table 1.

The cable capacitance is considered based on the cable data provided in [23], where the per-kilometer capacitance is reported as 0.16156 μF/km. By aggregating the two MMCs and the two cable capacitances, the total equivalent capacitance is calculated as $C = 645.42$ μF.

Similarly, the equivalent inductance is obtained by combining the cable inductance and the DCR inductance, taking into account the series-parallel configurations of the various DCRs and cables. The DCR inductance is 200 mH, and the per-kilometer cable inductance at the considered frequency range is 0.4 mH/km [23], resulting in a total inductance of $L = 320$ mH.

Finally, the resistance R is selected to reflect the resistive losses in the DC grid, which are mainly attributed to the cable resistance. According to [23], the per-kilometer resistance of the cable at the considered frequency is 0.04 Ω/km, yielding a total resistance of $R = 4$ Ω.

It should be noted that, to account for variations in grid configurations and parameters, a feasible range of the parameters of $Z^{dc}_{eq1}(s)$ can be selected to represent the grid impedance at the DC-PoC, given that only low-frequency dynamics are considered. An approach for analyzing such variations and determining the corresponding RLC parameters is presented in [28].

Fig. 17 compares the RLC model to the full grid model obtained in Section 2.2 for the three operating points defined

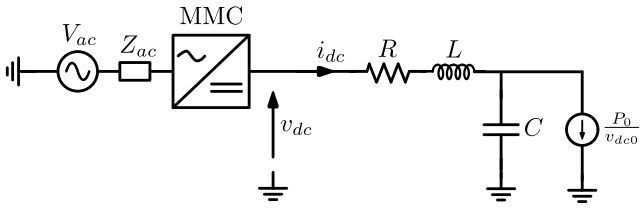

Figure 16: RLC equivalent model connected to the converter station.

in Section 3.2. The result confirms the capability of the RLC model to represent the grid impedance at the DC-PoC in a simplified form, considering different values of operating power in the DC grid. This equivalent representation can be used for the design of the converter control, or for the preliminary testing of the converter low-frequency response.

Moreover, it is possible to extend this RLC model in order to cover different control modes in the low-frequency range. For example, in Fig. 17, the control modes of the remote stations was considered in P-mode. If Station 2 is in droop control mode instead, a parallel circuit consisting of a DC voltage source in series with an RL element is added to the capacitor of the RLC model in Fig. 16, as shown in Fig. 18, in order to imitate the positive damping effect of droop control provided in the low-frequency range, as demonstrated in Section 3.2. The impedance of this extended representation can thus be written as

$$Z^{dc}_{eq2}(s) = R + sL + \frac{1}{sC - \frac{P_o}{v^2_{dc0}} + \frac{1}{sL_{droop}+R_{droop}}} \quad (5)$$

with R_{droop} being the parallel resistance representing the droop action provided by other converter stations in the DC grid. In fact, at steady state (i.e., $s = j0$), the grid impedance given in (5) reduces to

$$Z^{dc}_{eq2}(0) = R + \frac{R_{droop}}{1 - \frac{P_o R_{droop}}{v^2_{dc0}}}$$

which shows the steady-state impact of R_{droop} and the series resistance R, the latter representing the resistive losses in the DC grid, as well as the dependence on the operating point (P_o, v_{dc0}).

To choose the parameters in (5), the values of R, L, and C are selected as previously described for the simple RLC model in Section 4.1. R_{droop} is chosen to represent the droop action provided by Station 2, with a droop gain of $k_d = 0.1$ pu. Using the nominal DC voltage and power provided in Table 1, the droop resistance is calculated as $R_{droop} = \frac{k_d v^2_{dc0}}{P_{nom}} = 27.656\ \Omega$. The value of L_{droop} is selected to capture the dynamic effect of the droop control. It should be emphasized that L_{droop} does not necessarily represent a physical inductance in the grid. Instead, it is a dynamic term introduced to reflect the system's behavior around the low-frequency resonance, which is known to occur near 10 Hz. Based on this consideration, L_{droop} is set to 538 mH. If multiple droop-controlling stations are present in the grid, the value of R_{droop} can be adapted to reflect the aggregated effect of multiple droop controllers, following the principles of DC voltage droop characteristics, as discussed in [29, 28].

To verify this equivalent model, the extended RLC equivalent is compared to the actual grid impedance of Case 2 in Fig. 13. The results, depicted in Fig. 19, show that the RLC model accurately captures the low-frequency dynamics of the grid impedance, including the impact of the droop control mode of Station 2.

Depending on how the different converters in the grid operate and their respective control modes, the simplified RLC model thus far accommodates two possibilities for the control of remote stations:

- All stations in P-mode: A simple RLC equivalent, as shown in Fig. 16, can be used.
- One or more stations in droop control mode: An extended RLC equivalent, as shown in Fig. 18, can be applied. Here, R_{droop} and L_{droop} are chosen to represent both the steady-state and dynamic impacts of the droop control mode.

4.2. Frequency-dependent equivalent model

To further represent the grid impedance seen at the DC-PoC over a wider frequency range, a frequency-dependent equivalent model is proposed. This equivalent is obtained by fitting the actual grid impedance to a transfer function model. The order of this model can be selected based on the complexity of the grid impedance frequency response and the desired accuracy of the equivalent model. The vector fitting method in [30] is adapted to fit the grid impedance to a transfer function model of a predefined order.

Fig. 20 shows the approximation of the grid impedance using a 5^{th}-order transfer function. The results demonstrate that the two frequency responses are nearly identical, validating the proposed frequency-dependent equivalent model. It is important to note that the original DC-side impedance of the grid at the DC-PoC is of order 47, which is significantly reduced through the fitting process. This order reduction offers the advantage of allowing the equivalent model to be easily implemented in time-domain simulations, enabling it to capture the frequency-dependent grid dynamics while significantly reducing the computational burden associated with simulating the full grid model. This process will be further illustrated in the case study presented in Section 5.

The grid impedance of Case 2 (Station 2 operating in DC voltage droop control mode) is also fitted to a 5th-order transfer function. The results in Fig. 21 show that the frequency-dependent model can accurately capture the grid impedance dynamics while Station 2 operates in droop control mode. This is true for the three different grid operating points considered for Station 3.

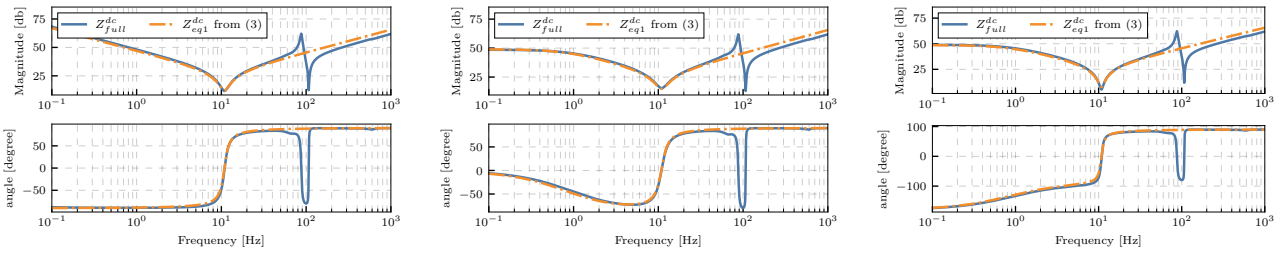

(a) op1 (b) op2 (c) op3

Figure 17: Validation of the RLC model against the full grid impedance when both remote stations are in P-mode following (3), with different operating points for St 2&3: (a) no power , (b) rectifier mode, and (c) inverter mode.

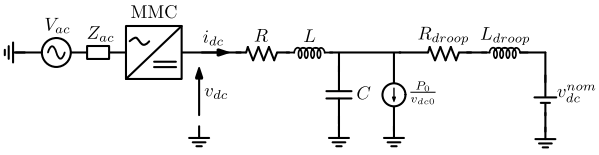

Figure 18: Extended RLC equivalent to cover droop control mode of station 2.

5. Case Study

This section focuses on time-domain simulations to validate the equivalent models obtained in Section 4 for the 3-terminal DC grid in Fig. 2. Subsequently, small-signal stability analysis is performed for a specific parameter set.

5.1. Time-domain simulations

5.1.1. Case 1

Station 1 in droop control mode regulates the DC voltage, with the droop gain k_d set to 0.05 pu. Stations 2 and 3 operate in constant P-mode, corresponding to Case 1 in Fig. 13. A 0.05 pu step increase in the DC voltage setpoint is applied to Station 1. Three models are tested:

1. The full 3-terminal grid model with MMCs modeled by the AAM, as shown in Fig. 2.
2. The RLC equivalent model, implemented according to Fig. 16.
3. The frequency-dependent grid model, where the grid impedance is fitted to a 5th-order transfer function. The implementation follows the schematic in Fig. 22.

The results in Fig. 23 show that both the RLC equivalent model and the frequency-dependent model can adequately represent the full grid dynamics in the low-frequency range, with the frequency-dependent model offering a more precise representation than the RLC model. This is true for all three operating points considered in Section 3.2.

Regarding the computational burden in the considered time-domain simulation, the full grid model requires approximately 2 minutes to simulate 5 seconds of operation, while both the RLC equivalent model and the fitted frequency-dependent model take around 19 seconds to simulate the same duration of operation. This demonstrates the significant computational efficiency of utilizing the equivalent models compared to simulating the full grid model.

5.1.2. Case 2

In Case 2 shown in Fig. 13, Station 2 operates in DC voltage droop control mode. The considered grid models are:

1. The full 3-terminal grid model with detailed MMC models, as shown in Fig. 2, with Station 2 operating in droop control mode.
2. The extended RLC equivalent model, shown in Fig. 18.
3. The frequency-dependent equivalent model implemented according to the setup in Fig. 22.

The results presented in Fig. 24 demonstrate that both the extended RLC equivalent and the frequency-dependent model accurately capture the static and dynamic responses of the full grid the step response. The impact of the droop control of Station 2 is also well captured.

5.2. Small-signal stability analysis

To evaluate the small-signal stability of the grid using the two proposed models, the impedance-based stability criterion is employed, which applies the Nyquist criterion on the open-loop transfer function to assess the stability of the closed-loop system in the frequency domain.

One potential source of instability in DC networks is the dynamic impact of the DC voltage droop gain. In this analysis, the droop gain of Station 1 is set to $k_d = 0.5\%$.

Fig. 25 presents the Bode plot of the Station 1 impedance Z_{MMC}, the equivalent RLC model Z^{dc}_{eq1}, and the return ratio defined as $L = \frac{ZMMC}{Z^{dc}_{eq1}}$. The return ratio represents the loop transfer function of the system, providing an indication of the system's closed-loop stability. The results show no intersection between the two impedance, indicating system stability. Furthermore, the Nyquist plot of L, depicted in Fig. 26, shows no encirclement of the -1 point, further confirming the stability of the system when the RLC model is utilized.

The same analysis is performed on the fitted equivalent model, where Z^{dc}_{fit} is used and the loop gain is redefined as $L = \frac{Z_{MMC}}{Z^{dc}_{fit}}$. The Bode plots are presented in Fig. 27,

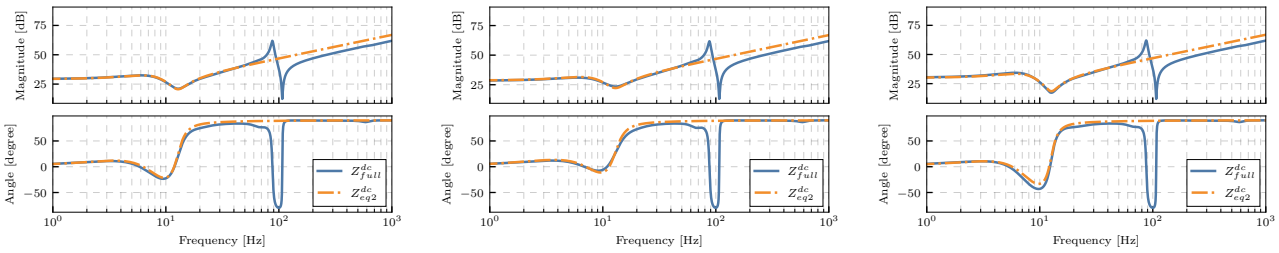

(a) op1 (b) op2 (c) op3

Figure 19: Validation of the extended RLC model against the full grid impedance when St 2 operates in Vdc droop following (5), with different operating points for St 3: (a) no power , (b) rated rectifier operation, and (c) rated inverter operation.

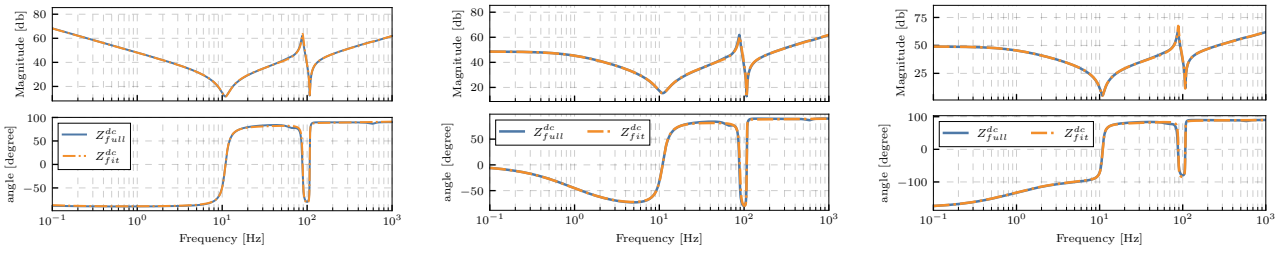

(a) op1 (b) op2 (c) op3

Figure 20: Comparison between the fitted grid impedance and the actual grid impedance when both remote stations are in P-mode, with different operating points for St 2&3: (a) no power , (b) rectifier mode, and (c) inverter mode.

and the Nyquist plot of L is shown in Fig. 28. The results demonstrate that the system is unstable, with a phase angle exceeding 180° at the gain crossover frequency $f_c = 110$ Hz in the Bode plot (Fig. 27) and a clockwise encirclement of the -1 point in the Nyquist plot (Fig. 28).

The case study results reveal that the RLC model provides an indication of the grid behavior only in the low-frequency range. In contrast, the frequency-dependent model accurately captures the high-frequency dynamics of the grid, which is critical for performing a thorough stability analysis of the system.

A time-domain simulation is conducted for the same case study to validate the small-signal analysis results, ensuring consistency by using the same physical and control parameters. The results with the full grid impedance, depicted in Fig. 29, confirm that the system is indeed unstable, and exhibits growing oscillations in the DC voltage at $f_c = 110$ Hz. This instability is reproduced with the frequency-dependent model, yielding oscillations at the same frequency, but not with the RLC model. These findings align with the predictions made by the small-signal analysis, and further validate the accuracy of the frequency-dependent model.

To demonstrate the applications of the two proposed models, Table 2 provides a comparison in terms of the required grid information, the order of the equivalent system, and the intended use of the two models. It is important to

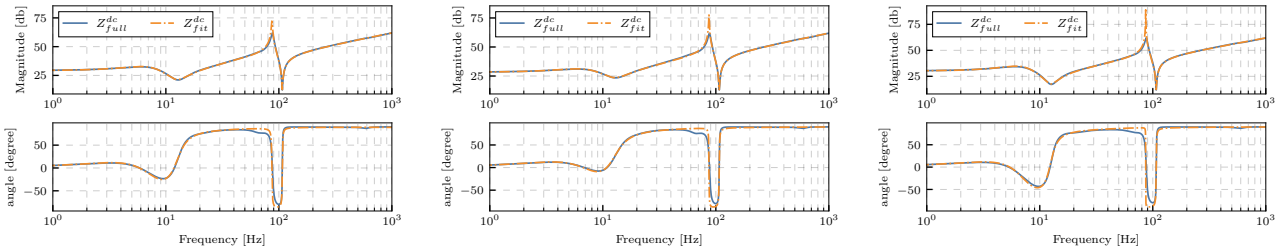

(a) op1 (b) op2 (c) op3

Figure 21: Comparison between the fitted grid impedance and the actual grid impedance for Case 2 (Station 2 operating in DC voltage droop control mode), with different operating points for St 3: (a) no power , (b) rated rectifier mode, and (c) rated inverter mode.

Table 2
Comparison between the two proposed DC equivalent models.

	RLC equivalent	**Frequency-dependent equivalent**
Required grid information	Minimal information needed, such as number of connected stations, DCR values, and cable length	The exact grid impedance at the DC-PoC, derived or scanned, is required to capture the response over the whole frequency range
Frequency range	Valid for dominant low-frequency dynamics	Valid for the entire frequency range 1-1000 Hz
Equivalent system order	second-order system	5th-order system (in the current grid configuration)
Application	Preliminary converter control design and testing.	Detailed stability analysis and final converter compliance testing.

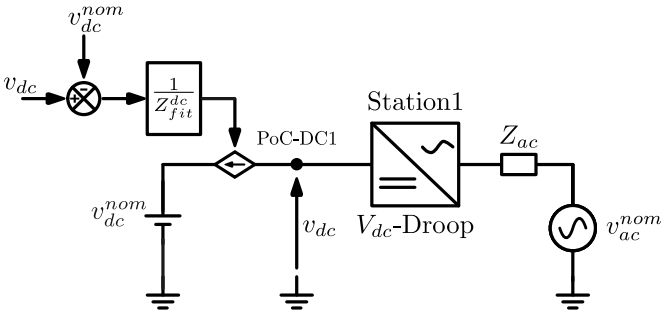

Figure 22: Implementation of the frequency-dependent grid impedance in time-domain simulation.

note that complete grid information is typically unavailable during the early stages of an HVDC project, particularly in multi-vendor MTDC grids. Therefore, to address uncertainties in grid conditions, converter manufacturers may aim for the simplified RLC model to test basic control functionalities. The frequency-dependent model becomes more appropriate when detailed grid data is available and a more accurate representation of grid dynamics is needed for stability analysis and final compliance testing. This approach aligns with the multi-vendor compliance testing recommendations outlined in [28].

Finally, it should be noted that the two proposed models can accurately represent the DC grid dynamics for testing the compliance of control functionalities within the frequency range considered. However, faster transient phenomena, such as DC-side faults, are not addressed in this paper, as they require additional analysis of the elements influencing the fault current, and the worst-case fault scenario. Reference [31] provides a comprehensive analysis of DC faults in MTDC grids, which can be utilized to develop equivalent models for fault studies.

6. Conclusions

In this paper, the dynamic behavior of a 3-terminal DC grid was investigated, with a focus on how various grid elements influence the impedance at the DC point of connection (DC-PoC). Through comparative analysis, it was shown that DC reactors, operating points, and the control modes of remote stations all have a significant impact on the grid's dynamic response across different frequency ranges.

To address the need for accurate yet practical representations of DC grid dynamics, two equivalent grid models were proposed. The first one, an RLC-based equivalent, provides a simple and effective method for capturing low-frequency behavior. It is particularly suitable for preliminary converter control design and low-frequency response testing. The second one, a frequency-dependent equivalent reduced from a higher-order model, captures both low- and high-frequency dynamics, offering a more comprehensive tool for detailed stability analysis.

Validation through frequency-domain impedance scans and comparison with nonlinear time-domain simulations confirmed the accuracy and reliability of both models. The results emphasize the importance of selecting the appropriate impedance representation based on the intended application and required accuracy. Furthermore, the frequency-dependent equivalent was successfully implemented in time-domain simulations, enabling the evaluation of small-signal stability conditions directly in the time domain.

Importantly, these equivalent models can also serve as a foundational step toward mitigating control interoperability challenges in MTDC systems by providing standardized and representative models for converter testing and control development in multi-vendor environments.

CRediT authorship contribution statement

Mohamed Elsodany: Writing - original draft, Investigation, Software, Methodology, Conceptualization. **Kosei Shinoda:** Writing - review & edit, Investigation, Methodology, Conceptualization. **Jing Dai:** Writing - review & edit, Investigation, Methodology, Conceptualization. **Seddik Bacha:** Writing - review & edit, Methodology, Conceptualization.

Declaration of Competing Interest

The authors declare that they have no known competing financial interests or personal relationships that could have appeared to influence the work reported in this paper.

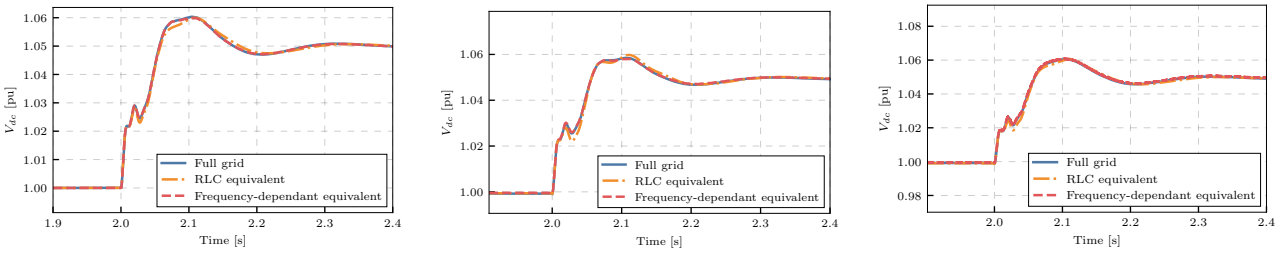

(a) DC voltage, op1 (b) DC voltage, op2 (c) DC voltage, op3

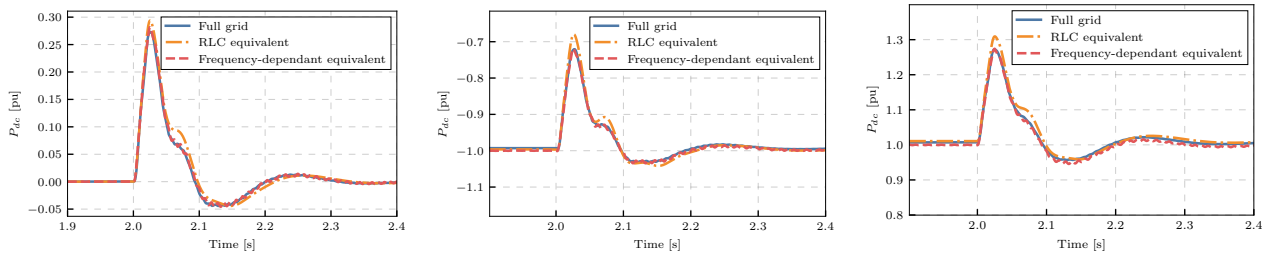

(d) DC power, op1 (e) DC power, op2 (f) DC power, op3

Figure 23: Step reference response of the DC voltage of Station 1 for the 3T grid model, the RLC model, and the frequency-dependent model.

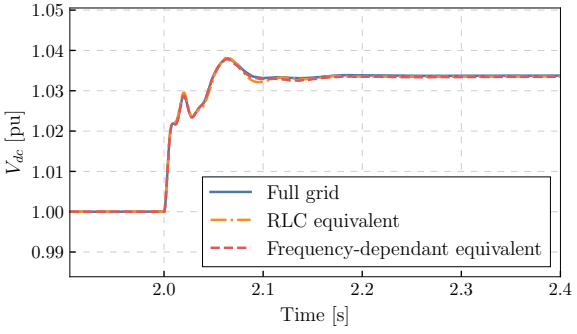

Figure 24: Step reference response of the DC voltage of Station 1 for the 3T grid model, the extended RLC model, and the frequency-dependent model.

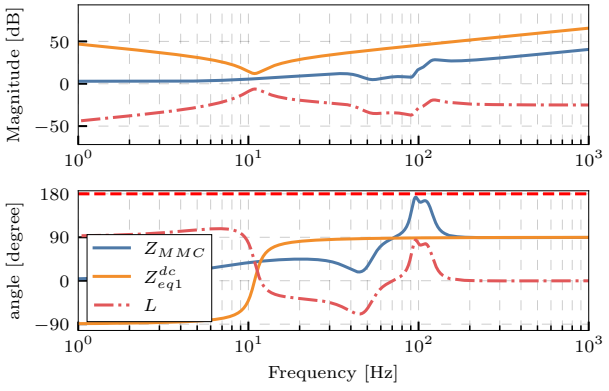

Figure 25: Bode plot of Z_{MMC}, Z_{eq1}, and the return ratio $L = \frac{Z_{MMC}}{Z^{dc}_{eq1}}$.

Acknowledgment

This paper includes research performed as a part of the InterOPERA Project under the grant agreement No 101095874 of the Horizon Europe Programme.

DISCLAIMER: Co-funded by the European Union. Views and opinions expressed are however those of the author(s) only and do not necessarily reflect those of the European Union or CINEA. Neither the European Union nor the granting authority can be held responsible for them.

A. DC grid impedance derivation

To derive the DC grid impedance at the DC Point of Connection (DC-PoC), the models of the MMC, cable, and DC reactors are derived and interconnected based on their input-output relationships.

MMC model

The state-space AAM of the MMC is adapted from [20] and shown in Fig. 3. The internal dynamics are represented by six equivalent arm capacitors C_{eq}, each in series with an inductance L_{arm} and resistance R_{arm}. The upper and lower arm variables, arm currents $i_k^{u,l}$, arm voltages $v_k^{u,l}$, capacitor voltages $v_{Ck}^{u,l}$, and modulation indices $m_k^{u,l}$, are transformed into Σ and Δ components as:

$$\begin{aligned} i_k^{\Sigma} &= \frac{i_k^u + i_k^l}{2}, & i_k^{\Delta} &= i_k^u - i_k^l \\ v_k^{\Sigma} &= \frac{v_k^u + v_k^l}{2}, & v_k^{\Delta} &= \frac{-v_k^u + v_k^l}{2} \end{aligned} \tag{6}$$

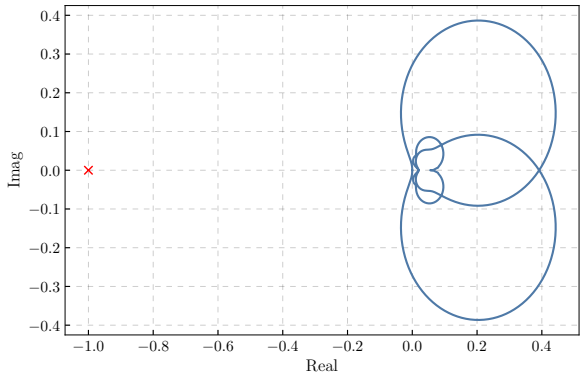

Figure 26: Nyquist plot of the return ratio $L = \frac{Z_{MMC}}{Z^{dc}_{eq1}}$

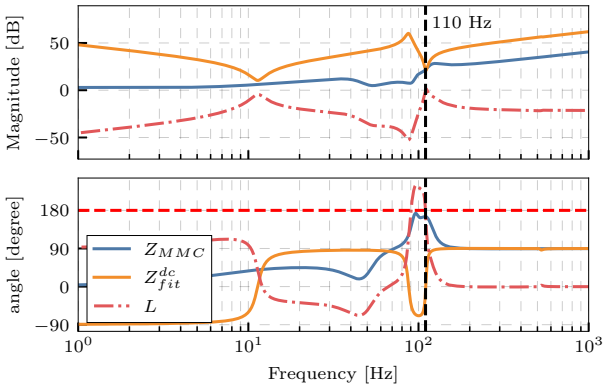

Figure 27: Bode plot of the Z_{MMC}, Z^{dc}_{fit}, and the return ratio $L = \frac{Z_{MMC}}{Z^{dc}_{fit}}$.

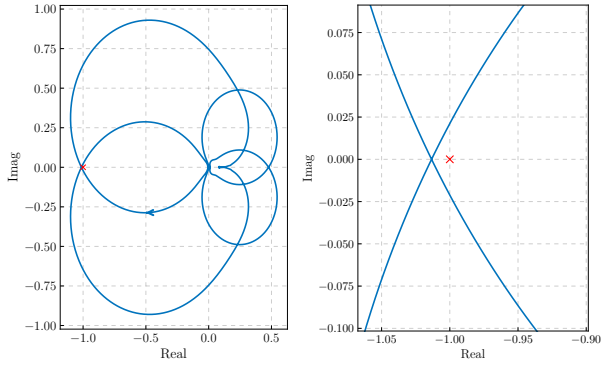

(a) (b)

Figure 28: (a) Nyquist plot of the return ratio $L = \frac{Z_{MMC}}{Z^{dc}_{fit}}$ (b) Zoomed plot.

$$
\begin{aligned}
v^{\Sigma}_{Ck} &= \frac{v^{u}_{Ck} + v^{l}_{Ck}}{2}, & v^{\Delta}_{Ck} &= \frac{v^{u}_{Ck} - v^{l}_{Ck}}{2} \\
m^{\Sigma}_{k} &= m^{u}_{k} + m^{l}_{k}, & m^{\Delta}_{k} &= m^{u}_{k} - m^{l}_{k}
\end{aligned} \tag{7}
$$

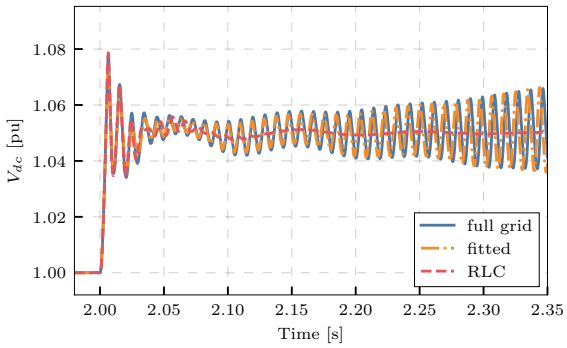

Figure 29: A 0.05 step change in the DC voltage setpoint of Station 1 is applied at $t = 2$s.

Co-funded by the European Union

Here, i^{Σ}_{k} is the common-mode circulating current driven by v^{Σ}_{k}, while i^{Δ}_{k} is the output current driven by v^{Δ}_{k}. The voltages v^{Σ}_{Ck} and v^{Δ}_{Ck} respectively represent the capacitor voltages in Σ and Δ form, and m^{Σ}_{k} and m^{Δ}_{k} are the corresponding modulation indices.

The governing equations in the Σ-Δ domain are:

$$
\begin{aligned}
L_{ac}\frac{di^{\Delta}_{k}}{dt} &= v^{\Delta}_{k} - v^{g}_{k} - R_{ac}i^{\Delta}_{k} \\
L_{arm}\frac{di^{\Sigma}_{k}}{dt} &= \frac{v_{dc}}{2} - v^{\Sigma}_{k} - R_{arm}i^{\Sigma}_{k} \\
2C_{eq}\frac{dv^{\Delta}_{Ck}}{dt} &= m^{\Sigma}_{k}\frac{i^{\Delta}_{k}}{2} + m^{\Delta}_{k}i^{\Sigma}_{k} \\
2C_{eq}\frac{dv^{\Sigma}_{Ck}}{dt} &= m^{\Delta}_{k}\frac{i^{\Delta}_{k}}{2} + m^{\Sigma}_{k}i^{\Sigma}_{k}
\end{aligned} \tag{8}
$$

where $L_{ac} = L_{tr} + \frac{L_{arm}}{2}$ and $R_{ac} = R_{tr} + \frac{R_{arm}}{2}$ denote the equivalent AC-side inductance and resistance.

Applying the Park transformation to (8) yields the steady-state time-invariant dq model. The resulting state variables in the dq frame are: i^{Δ}_{d}, i^{Δ}_{q}, i^{Σ}_{d}, i^{Σ}_{q}, i^{Σ}_{z}, v^{Δ}_{Cd}, v^{Δ}_{Cq},v^{Σ}_{Cd}, v^{Σ}_{Cq}, and v^{Σ}_{Cz}, v^{Δ}_{CZd}, v^{Δ}_{CZq}.

MMC control

According to the MMC control structure shown in Fig. 4 and described in Section 2.1, the integrator state of each PI controller (2 for the AC current, 2 for the circulating current, 1 for the active power) is denoted ϵ_x, and governed by:

$$
\frac{d\epsilon_x}{dt} = k^{x}_{i}(x^{*} - x)
$$

The full linearized MMC model in the dq frame, including control dynamics, is of order 17. The state vector is:

$$
\begin{aligned}
\vec{x}_{MMC} = [&i^{\Delta}_{d},\ i^{\Delta}_{q},\ i^{\Sigma}_{d},\ i^{\Sigma}_{q},\ i^{\Sigma}_{z},\ v^{\Delta}_{Cd},\ v^{\Delta}_{Cq},\ v^{\Sigma}_{Cd}, \\
&v^{\Sigma}_{Cq},\ v^{\Sigma}_{Cz},\ v^{\Delta}_{CZd},\ v^{\Delta}_{CZq},\ \epsilon_{i^{\Delta}_{d}}, \\
&\epsilon_{i^{\Delta}_{q}},\ \epsilon_{i^{\Sigma}_{d}},\ \epsilon_{i^{\Sigma}_{q}},\ \epsilon_{P}]^{T} \in \mathbb{R}^{17}
\end{aligned}
$$

Table 3
Fitting coefficients of the admittance $Y_{fit}^{dc}(s)$ for op1 in Fig. 20.

Coeff.	a_4	a_3	a_2	a_1	a_0
Value	263.1	4.626×10^5	1.177×10^8	3.36×10^9	5.225×10^{11}
Coeff.	b_4	b_3	b_2	b_1	b_0
Value	5.027	1136	1.581×10^6	3.244×10^8	1.092×10^7

Table 4
Fitting coefficients of the admittance $Y_{fit}^{dc}(s)$ for op2 in Fig. 20.

Coeff.	a_4	a_3	a_2	a_1	a_0
Value	372.3	4.669×10^5	1.678×10^8	4.895×10^9	7.529×10^{11}
Coeff.	b_4	b_3	b_2	b_1	b_0
Value	5.027	1662	1.621×10^6	4.766×10^8	2.791×10^7

Table 5
Fitting coefficients of the admittance $Y_{fit}^{dc}(s)$ for op3 in Fig. 20.

Coeff.	a_4	a_3	a_2	a_1	a_0
Value	144.6	4.6×10^5	8.641×10^7	2.534×10^9	3.837×10^{11}
Coeff.	b_4	b_3	b_2	b_1	b_0
Value	5.023	806.9	1.554×10^6	2.299×10^8	-1.358×10^9

Table 6
Fitting coefficients of the admittance $Y_{fit}^{dc}(s)$ for Case 2 in Fig. 21, considering no power operation of Station 3.

Coeff.	a_4	a_3	a_2	a_1	a_0
Value	71.13	4.605×10^5	2.91×10^7	3.249×10^9	9.762×10^{10}
Coeff.	b_4	b_3	b_2	b_1	b_0
Value	5.008	218.1	1.5×10^6	6.088×10^7	3.362×10^9

Table 7
Fitting coefficients of the admittance $Y_{fit}^{dc}(s)$ for Case 2 in Fig. 21, considering rectifier operation for Station 3.

Coeff.	a_4	a_3	a_2	a_1	a_0
Value	82.08	4.61×10^5	3.387×10^7	3.452×10^9	9.647×10^{10}
Coeff.	b_4	b_3	b_2	b_1	b_0
Value	5.011	270.8	1.508×10^6	7.485×10^7	3.685×10^9

Cable and DCR models

The cable model, shown in Fig. 5, is linear and represented by the dynamic equations of inductors and capacitors. The state vector is:

$$\vec{x}_{cable} = [i_{l1},\ i_{l2},\ i_{l3},\ v_{c1},\ v_{c2}]^T \in \mathbb{R}^5$$

The DC reactors (DCRs) are modeled as single inductors, leading to a first-order system for each DCR.

Grid impedance

To compute the DC grid impedance as seen from DC-PoC1, the full state-space model is constructed by interconnecting the MMC, cable, and DCR models. The full systems state vector is:

$$\vec{x}_{full} = [\vec{x}_{MMC2}^T,\ \vec{x}_{MMC3}^T,\ \vec{x}_{cable1}^T,\ \vec{x}_{cable2}^T,\ i_{DCR1},\ i_{DCR2},\ i_{DCR3}]^T \in \mathbb{R}^{47}$$

From the above state-space model, and following the approach in Fig. 6, the grid admittance $Y_{grid}(s)$ at DC-PoC1 is derived, and the grid impedance is obtained as

$$Z_{grid} = \frac{1}{Y_{grid}(s)}$$

with a complete system of order 47th.

B. Fitting results of the grid impedance

In this appendix, the fitted transfer function of the grid impedance is presented according to the procedure described in Section 4.2. The grid impedance shown in Fig. 20 is approximated using a 5th-order transfer function. Note that we first fit the admittance $Y_{grid}(s)$, and then take its inverse to obtain the impedance $Z_{fit}^{dc}(s)$. The fitted transfer function of the admittance for op1 is given by:

$$Y_{fit}^{dc}(s) = \frac{b_4 s^4 + b_3 s^3 + b_2 s^2 + b_1 s + b_0}{s^5 + a_4 s^4 + a_3 s^3 + a_2 s^2 + a_1 s + a_0}$$

with the coefficients provided in Tables 3, 4, 5 for the three operating points considered in Fig. 20

Similarly, the coefficients of the fitted grid admittance for Case 2 in Fig. 21 are provided in Tables 6,7 and 8 .

References

[1] B. Luscan, S. Bacha, A. Benchaib, A. Bertinato, L. Chedot, J. C. Gonzalez-Torres, S. Poullain, M. Romero-Rodriguez, K. Shinoda, A vision of hvdc key role toward fault-tolerant and stable ac/dc grids, IEEE Journal of Emerging and Selected Topics in Power Electronics 9 (2021) 7471–7485.

[2] J. Beerten, S. D'Arco, J. A. Suul, Identification and Small-Signal Analysis of Interaction Modes in VSC MTDC Systems, IEEE Transactions on Power Delivery 31 (2016) 888–897.

[3] Q. Fu, W. Du, H. Wang, B. Ren, X. Xiao, Small-Signal Stability Analysis of a VSC-MTDC System for Investigating DC Voltage Oscillation, IEEE Transactions on Power Systems 36 (2021) 5081–5091.

[4] X. Lu, W. Xiang, W. Lin, J. Wen, Small-signal modeling of mmc based dc grid and analysis of the impact of dc reactors on the small-signal stability, International Journal of Electrical Power and Energy Systems 101 (2018) 25–37.

[5] T. Roose, A. Lekic, M. M. Alam, J. Beerten, Stability analysis of high-frequency interactions between a converter and hvdc grid resonances, IEEE Transactions on Power Delivery 36 (2021) 3414–3425.

[6] Y. Liao, H. Wu, X. Wang, M. Ndreko, R. Dimitrovski, W. Winter, Stability and Sensitivity Analysis of Multi-Vendor, Multi-Terminal HVDC Systems, IEEE Open Journal of Power Electronics 4 (2023) 52–66.

[7] A. J. Agbemuko, J. L. Domínguez-García, E. Prieto-Araujo, O. Gomis-Bellmunt, Dynamic modelling and interaction analysis of multi-terminal vsc-hvdc grids through an impedance-based approach, International Journal of Electrical Power and Energy Systems 113 (2019) 874–887.

[8] A. Ibrahim, Frequency dependent network equivalents for electromagnetic transients studies: a bibliographical survey, International Journal of Electrical Power and Energy Systems 25 (2003) 193–199.

[9] A. Bayo-Salas, J. Beerten, D. Van Hertem, Analytical methodology to develop frequency-dependent equivalents in networks with multiple converters, in: 2017 IEEE Manchester PowerTech, IEEE, 2017. doi:10.1109/ptc.2017.7980938.

Table 8
Fitting coefficients of the admittance $Y_{fit}^{dc}(s)$ for Case 2 in Fig. 21, considering inverter operation for Station 3.

Coeff.	a_4	a_3	a_2	a_1	a_0
Value	60.54	4.601×10^5	2.44×10^7	3.053×10^9	9.872×10^{10}
Coeff.	b_4	b_3	b_2	b_1	b_0
Value	5.002	166.7	1.488×10^6	4.785×10^7	3.054×10^9

[10] W. C4.56, Electromagnetic transient simulation models for large-scale system impact studies in power systems having a high penetration of inverter-connected generation, Technical Report TB881, CIGRE, 2022.

[11] C. Buchhagen, C. Rauscher, A. Menze, J. Jung, Borwin1 - first experiences with harmonic interactions in converter dominated grids, in: International ETG Congress 2015, 2015.

[12] E. Commission, Commission regulation (eu) 2016/1447 of 26 august 2016 establishing a network code on requirements for grid connection of high voltage direct current systems and direct current-connected power park modules, Official Journal of the European Union (2016).

[13] E. Prieto-Araujo, A. Egea-Alvarez, S. Fekriasl, O. Gomis-Bellmunt, DC Voltage Droop Control Design for Multiterminal HVDC Systems Considering AC and DC Grid Dynamics, IEEE Transactions on Power Delivery 31 (2016) 575–585.

[14] J. Beerten, Modeling and Control of DC Grids, Ph.D. thesis, KU Leuven, 2013.

[15] J. Freytes, P. Rault, F. Gruson, F. Colas, X. Guillaud, Dynamic impact of mmc controllers on dc voltage droop controlled mtdc grids, in: 2016 18th European Conference on Power Electronics and Applications (EPE'16 ECCE Europe), IEEE, 2016, pp. 1–10. doi:10.1109/epe.2016.7695423.

[16] K. Shinoda, A. Benchaib, J. Dai, X. Guillaud, Virtual Capacitor Control: Mitigation of DC Voltage Fluctuations in MMC-Based HVdc Systems, IEEE Transactions on Power Delivery 33 (2018) 455–465.

[17] F. Ahmadloo, S. P. Azad, Identifying suitable DC system models for an independent design of VSC controllers in MTDC grids, International Journal of Electrical Power and Energy Systems 153 (2023) 109380.

[18] H. Saad, S. Dennetiere, J. Mahseredjian, P. Delarue, X. Guillaud, J. Peralta, S. Nguefeu, Modular Multilevel Converter Models for Electromagnetic Transients, IEEE Transactions on Power Delivery 29 (2014) 1481–1489.

[19] A. Zama, S. Bacha, A. Benchaib, D. Frey, S. Silvant, A novel modular multilevel converter modelling technique based on semi-analytical models for HVDC application, Journal of Electrical Systems (2016).

[20] G. Bergna-Diaz, J. Freytes, X. Guillaud, S. D'Arco, J. A. Suul, Generalized Voltage-Based State-Space Modeling of Modular Multilevel Converters With Constant Equilibrium in Steady State, IEEE Journal of Emerging and Selected Topics in Power Electronics 6 (2018) 707–725.

[21] Q. Tu, Z. Xu, L. Xu, Reduced Switching-Frequency Modulation and Circulating Current Suppression for Modular Multilevel Converters, IEEE Transactions on Power Delivery 26 (2011) 2009–2017.

[22] J. Beerten, S. D'Arco, J. Suul, Cable Model Order Reduction for HVDC Systems Interoperability Analysis, in: 11th IET International Conference on AC and DC Power Transmission, Institution of Engineering and Technology, 2015. doi:10.1049/cp.2015.0039.

[23] J. Freytes, Small-signal stability analysis of Modular Multilevel Converters and application to MMC-based Multi-Terminal DC grids, Ph.D. thesis, CENTRALE LILLE, 2017.

[24] M. Barnes, D. S. Vilchis-Rodriguez, X. Pei, R. Shuttleworth, O. Cwikowski, A. C. Smith, HVDC Circuit Breakers–A Review, IEEE Access 8 (2020) 211829–211848.

[25] Y. Wang, X. Wang, Z. Chen, F. Blaabjerg, Small-Signal Stability Analysis of Inverter-Fed Power Systems Using Component Connection Method, IEEE Transactions on Smart Grid 9 (2018) 5301–5310.

[26] W. Wang, M. Barnes, O. Marjanovic, O. Cwikowski, Impact of DC Breaker Systems on Multiterminal VSC-HVDC Stability, IEEE Transactions on Power Delivery 31 (2016) 769–779.

[27] M. Cespedes, L. Xing, J. Sun, Constant-power load system stabilization by passive damping, IEEE Transactions on Power Electronics 26 (2011) 1832–1836.

[28] P. Torwelle, K. Shinoda, P. Verrax, A. Bertinato, H. F. de Barros, D. Gomez-Acero, M. Elsodany, E. Witz, A. Saçıak, Functional requirements for HVDC grid systems and subsystems, Deliverable D2.1, InterOPERA, 2024. URL: https://interopera.eu/publications/, [Online].

[29] K. Shinoda, A. Benchaib, J. Dai, X. Guillaud, Over- and under-voltage containment reserves for droop-based primary voltage control of mtdc grids, IEEE Transactions on Power Delivery 37 (2022) 125–135.

[30] B. Gustavsen, A. Semlyen, Rational approximation of frequency domain responses by vector fitting, IEEE Transactions on Power Delivery 14 (1999) 1052–1061.

[31] M. Abedrabbo, F. Z. Dejene, W. Leterme, D. Van Hertem, Hvdc grid post-dc fault recovery enhancement, IEEE Transactions on Power Delivery 36 (2021) 1137–1148.